

Estimates of Dissipation in the Ocean Mixed Layer Using a Quasi-Horizontal Microstructure Profiler

BLAIR J. W. GREENAN, NEIL S. OAKEY, AND FRED W. DOBSON

Ocean Sciences Division, Bedford Institute of Oceanography, Maritimes Region, Fisheries and Oceans Canada, Dartmouth, Nova Scotia, Canada

(Manuscript received 1 March 2000, in final form 7 July 2000)

ABSTRACT

Some recent measurements of the mixed layer in oceans and lakes have indicated that the rate of the dissipation of turbulent kinetic energy, ϵ , is much higher than expected from a purely shear-driven wall layer. This enhancement has usually been attributed to wave breaking. In this study, measurements of dissipation in the open-ocean mixed layer on the continental shelf off Nova Scotia are integrated with air-sea flux estimates and directional wave spectra to further study this issue. A microstructure profiler gliding quasi-horizontally provides estimates of ϵ starting within 2 m of the ocean surface as it slowly descends through the mixed layer. Dissipation rates were found to be enhanced relative to the wind stress production and indicated that $\sim 6\%$ of the wind energy at 10 m is dissipated in the ocean mixed layer. In addition, results from this experiment demonstrate that the WAVES scaling for ϵ , based on wind and wave parameters, is valid for the case of a simple windsea in which the swell can be easily separated. In more complex wave conditions ϵ remains enhanced relative to the classical wall layer; however, the WAVES scaling does not hold.

1. Introduction

The ocean mixed layer (OML) is defined as the region of the upper ocean directly influenced by surface mixing processes. This layer is bounded by the ocean's surface on top and by the pycnocline at the bottom. The predominant seasonal and daily cycles in this layer originate at the ocean surface. Forcing variables for the OML are primarily solar heating, wind stress, and vertical fluxes of latent and sensible heat. Nevertheless, in some circumstances precipitation or evaporation can cause convective instability while internal waves at the base of the mixed layer can generate shear instabilities.

The near-surface distribution of the rate of turbulent kinetic energy dissipation, ϵ , has been the subject of considerable research in recent years and, yet, the results remain inconclusive. The difficulty associated with acquiring near-surface data in the OML combined with the intermittent nature of small-scale turbulent processes has made it difficult to obtain statistically robust results. In general, the results of these studies have been categorized as either 1) demonstrating agreement with the structure of a classical shear-driven wall layer expected from similarity scaling or 2) having dissipation values

substantially higher than anticipated. The results in the latter group are usually attributed to enhanced dissipation caused by wave breaking.

Some studies (Dillon et al. 1981; Oakey and Elliott 1982; Soloviev et al. 1988) have shown that wind-driven near-surface layers exhibit scaling laws consistent with constant stress layers over solid boundaries. In these cases the dissipation of turbulent kinetic energy, $\epsilon(z)$, scales with depth, z , as $u_{*w}^3/\kappa z$, where κ is von Kármán's constant (0.4) and u_{*w} is the friction velocity in water. To support this view, Churchill and Csanady (1983) report the existence of logarithmic mean current profiles in the surface boundary layer. Jones and Kenney (1977) found that the turbulent velocity fluctuations have a velocity scale proportional to the friction velocity in water and a length scale proportional to depth. Using data collected in a convective ocean mixed layer, Lombardo and Gregg (1989) concluded that ϵ scaled with the sum of the convective and surface-layer scalings.

In contrast to the results supporting the assumption of a constant stress layer in the near surface, there have been an increasing number of studies indicating that turbulence and mixing are enhanced relative to the wind stress production. Surface layer measurements in Lake Ontario have provided evidence of enhanced levels of turbulence, which have been attributed to wave breaking (Kitaigorodskii et al. 1983; Agrawal et al. 1992). Subsequent work by Terray et al. (1996, hereafter T96) showed that within one significant wave height of the

Corresponding author address: Dr. Blair J. W. Greenan, Ocean Sciences Division, Bedford Institute of Oceanography, P.O. Box 1006, Dartmouth, NS B2Y 4A2, Canada.
E-mail: greenanb@mar.dfo-mpo.gc.ca

surface, dissipation is an order of magnitude higher than that predicted by wall layer theory. Below this was found to be an intermediate region where dissipation decays as z^{-2} and at sufficient depth the dissipation asymptotes to the expected wall layer values. Terray et al. proposed a wave-dependent scaling of the dissipation rate based on the significant wave height and the rate of energy input from the wind to the waves.

Further support for elevated turbulence levels in the aquatic surface layer has also been established by several ocean studies (Gregg 1987; Gargett 1989; Osborn et al. 1992; Anis and Moum 1992, 1995; Drennan et al. 1996; Gemmrich and Farmer 1999). Using a submarine-based platform, Osborn et al. (1992) combined turbulence measurements from shear probes with observations of bubble clouds. This study provided evidence of high dissipation in bubble clouds resulting from wave breaking. Using a vertically rising profiler in the mixed layer, Anis and Moum (1995, hereafter AM95) found that in situations in which dissipation was greatly enhanced relative to the wind stress production, ε exhibited an exponential decay with depth. They suggested two possible mechanisms to explain the behavior of ε near the surface: 1) the high level of turbulent kinetic energy created by wave breaking at the surface is transported downward away from the surface by the orbital motion of the swell and 2) energy drawn from a rotational wave field to the mean flow, via the wave stresses, is in turn drawn from the mean flow by the turbulence production term, which is balanced by ε . Drennan et al. (1996) employed a shipborne current meter during the Surface Waves Dynamics Experiment (SWADE) to estimate dissipation at 2 m below the ocean surface. Their results support the wave-dependent scaling of dissipation rate as proposed by T96. Using a freely drifting instrument, Gemmrich and Farmer (1999) made inferences about ocean surface turbulence through the measurement of the near-surface temperature structure. These results demonstrated the presence of wave-enhanced turbulence as well as subsurface advection due to Langmuir circulation.

The results presented here include measurements of dissipation in the ocean mixed layer using a combination of vertical and quasi-horizontal microstructure profilers. A shipboard-mounted bow-anemometer system provided air-sea flux measurements. Wave spectra were measured with a Waverider pitch/roll buoy. This comprehensive set of measurements will allow us to further investigate the wave-dependent scaling of dissipation rate as proposed by T96. The following section describes the instrumentation and field experiment. The data analysis procedure is explained in section 3. The experiment results are discussed in section 4. Conclusions and a summary are presented in section 5.

2. Field experiment

This study is based on a field experiment conducted at Emerald Bank on the Scotian Shelf in a relatively

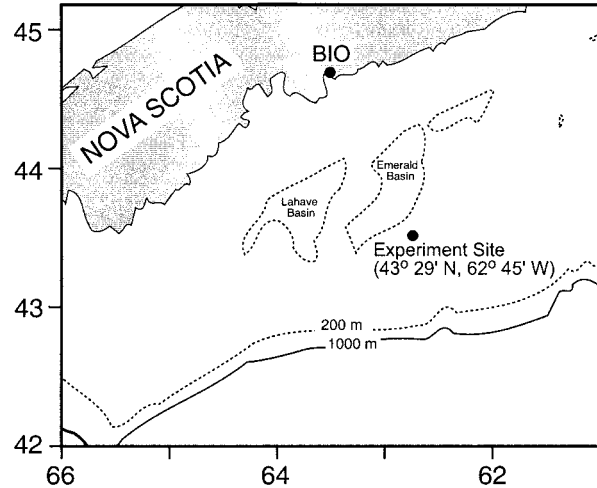


FIG. 1. Location of the Emerald Bank experiment, 17–30 Jun 1996.

level area of water 100 m deep (Fig. 1). The experiment was carried out on the CSS *Parizeau* from 17 to 30 June 1996. Two microstructure profilers were used to provide both vertical and quasi-horizontal microscale measurements of velocity shear and temperature fluctuations. Both profilers use a similar suite of microstructure sensors including airfoil shear probes, an FP07 fast thermistor, and a DISA platinum thin film sensor. Data collected with these instruments was used to calculate the dissipation of turbulent kinetic energy, ε , and the dissipation of thermal variance, χ_T .

The tethered free-fall vertical profiler, EPSONDE2 (Oakey 1988), was deployed from the foredeck of the CSS *Parizeau* and provided data from within 5 m of the surface to the seabed. At a drop speed of ~ 0.8 m s^{-1} , this instrument provided estimates of mixing parameters with approximately 1.5-m resolution in the vertical. A total of 324 profiles were collected during the experiment.

The quasi-horizontal profiler, EPSONDE-Glider (Greenan and Oakey 1999), was used for the first time during this experiment. The instrument is a tethered free-fall glider developed to provide a more comprehensive set of microstructure measurements in the mixed layer, a segment of the water column that vertical profilers typically do not sample very well. The chassis of the vehicle incorporates a cambered main wing (span 2.43 m, chord 0.43 m) to provide lift and a symmetrical elevator wing (span 1.22 m, chord 0.25 m) to control glide angle. The motive force of the vehicle is provided by a ballast weight that can be detached from the vehicle to make it positively buoyant in case of an emergency. The instrument payload is very similar to that of the vertical profiler. A data link to the ship and vehicle tether is provided by a 1000 m, four-conductor Kevlar cable. The EPSONDE-Glider profiled along a flight path with a glide angle of (typically) 12° in the ocean mixed layer. At a speed of ~ 0.5 m s^{-1} , it provided estimates of

mixing parameters with approximately 0.75-m resolution in the vertical. A total of 75 profiles was collected during the experiment.

Measurements in the atmospheric boundary layer were collected with a moored Coastal Climate Minimet buoy and a bow anemometer system on the CSS *Parizeau*. The Minimet buoy, deployed at 43°30.3'N, 62°44.4'W, provided atmospheric pressure, air and sea temperature, and wind speed and direction at 3.3 m above sea level at 30-min intervals. The bow anemometer system (Dobson et al. 1994) consists of a mast at the ship's bow carrying an RM Young Wind Monitor RE propeller-vane anemometer and two fast-response air temperature thermistors mounted 13 m above the waterline. Sea surface wind stress and heat flux were calculated using an inertial-dissipation method (Anderson 1993). If temperature fluctuation data fail to meet the criteria of this method, the heat flux was estimated from wind speed and air-sea temperature difference by a bulk method (Smith 1980).

Wave measurements were collected with a Datawell Waverider directional wave buoy (DWR) deployed at 43°29.0'N, 62°44.9'W. The buoy is a 0.9-m diameter aluminum sphere floating on the sea surface and moored to the bottom with an elastic tether. It uses a flux-gate compass and three accelerometers to determine the first five Fourier coefficients of the full wave directional spectrum, $F(\omega, \theta)$, where ω is radian frequency and θ is wave direction. The wave data are sampled every 0.781 25 sec and the spectra calculated by FFT over eight 256 data point blocks, making the run length 20 min, the basic frequency resolution 0.005 Hz, and the Nyquist frequency 0.64 Hz. The wave data including the Fourier coefficients are radio-telemetered from the buoy to the attending ship. The Fourier coefficients are processed using the "MEM" (maximum entropy method) technique (Lygre and Krogstad 1986) to produce the full wave directional spectra $F(\omega, \theta)$ presented here.

3. EPSONDE data analysis

A simplified form of the turbulent kinetic energy equation for the ocean mixed layer can be expressed as

$$\frac{d}{dt} \left(\frac{1}{2} \overline{q^2} \right) = -\overline{u'w'} \frac{\partial \bar{u}}{\partial z} - \varepsilon - g \frac{\overline{\rho'w'}}{\rho}, \quad (1)$$

where the term on the left is the time rate of change of mean turbulent kinetic energy (TKE) per unit mass. The first term on the right is the rate of production of TKE by Reynolds stress working against the mean shear and ε is the rate of dissipation. The final term is the rate of change of potential energy through the buoyancy flux.

The rate of dissipation is defined as $\varepsilon \equiv 2\nu \overline{s_{ij} s_{ij}}$, where s_{ij} is the fluctuating rate of strain and ν is the kinematic viscosity. If isotropy is assumed, ε is given by

$$\varepsilon = \frac{15}{2} \nu \left(\frac{du'}{dz} \right)^2. \quad (2)$$

The time derivative signals from the instrument shear probes are converted to spatial derivatives by making use of the nearly constant instrument speed and Taylor's hypothesis.

Estimates of dissipation from both the vertical profiler and the glider were obtained using a similar set of processing software. The only major difference in the two datasets was that instrument speed was determined from the pressure gradient signal for the EPSONDE2 profiler, while the speed of EPSONDE-Glider was obtained from a wing-mounted impeller flowmeter.

Each instrument was equipped with two shear probes. The shear probes on the vertical profiler were oriented parallel to one another, while the glider probes were perpendicular to one another and measured a vertical and horizontal component. In practice, ε was obtained from the average of the shear measured by two probes. Two scatter diagrams (Fig. 2) show the self-consistency of the two shear probes for both instruments. The EPSONDE-Glider has a noise level of $1 \times 10^{-9} \text{ W kg}^{-1}$, while the vertical profiler noise level is approximately $2 \times 10^{-10} \text{ W kg}^{-1}$. This noise level for the glider is sufficient to make accurate measurements of dissipation in the mixed layer.

The fact that the orbital wave velocities are high compared to the turbulence velocities might lead to misgivings about measurement of TKE dissipation rate in the near-surface wave zone. One significant point to note is that our turbulence sensors measure only velocity fluctuations and are not sensitive to velocities with a period of more than about 1 second. Nevertheless, errors in measurement that might occur in the wave zone are worthy of a brief discussion. The shear probe sensors and sources of nonlinearity are described in detail in Osborn and Crawford (1980). The sensor is a pointed axially symmetric foil of revolution for which the principal response in normal operation is the force caused by potential flow (at small angles of attack) proportional to the product of the axial flow (V) and the perpendicular off-axis turbulent flow (u). If this were the only force, the sensor would be linear and, in fact, this is a good approximation for deep ocean measurements where there is little off-axis mean flow. Nevertheless, there is a second force due to viscous effects, proportional to the square of the cross-stream velocity which increases with increasing angle of attack. This force may lead to apparent measurement nonlinearity in conditions such as the near surface where the instrument that carries the sensor does not follow the wave orbital velocity well and the sensor experiences off-axis mean flows large compared to the velocity of the instrument. Under normal conditions we would consider that for angles of attack of less than $\pm 20^\circ$ that the sensor is linear within the ability to calibrate it (of order $\pm 5\%$). With a glider speed of 0.5 m s^{-1} through the water this $\pm 20^\circ$ limit is reached with an off-axis flow of order 0.18 m s^{-1} . For a 5-s wind wave of 1-m amplitude, the maximum orbital water velocity perpendicular to a fixed profiler would

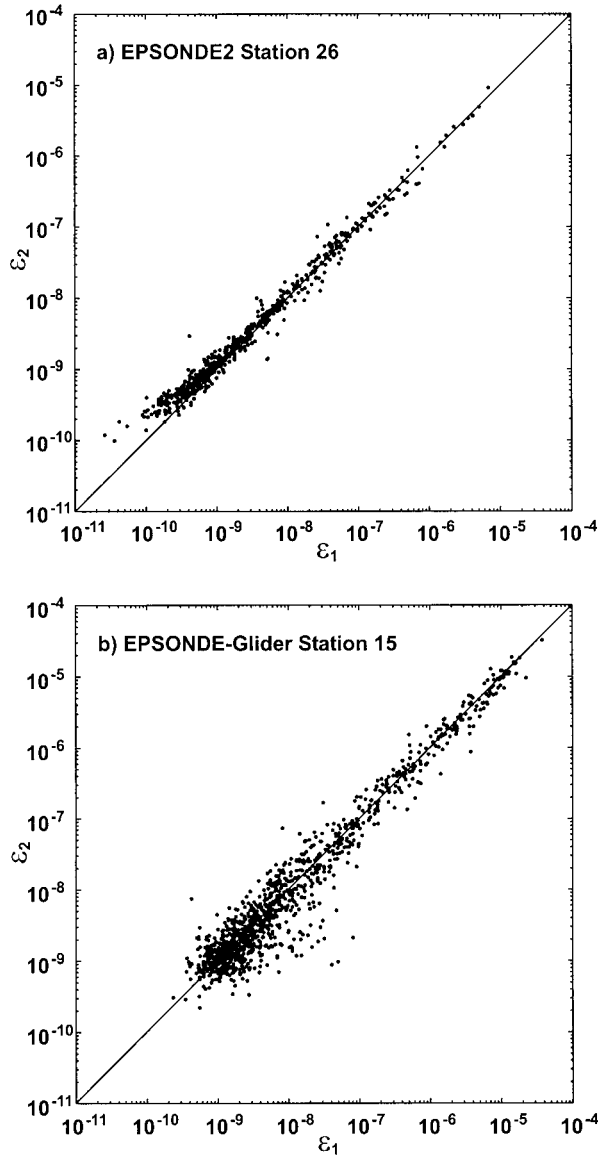


FIG. 2. Comparison of ϵ for all profiles in a station as estimated by each shear probe on (a) EPSONDE2 and (b) EPSONDE-Glider. Each data point represents an estimate of ϵ for an individual segment (1.5 m for EPSONDE2 and 0.75 m for EPSONDE-Glider).

be at or higher than this level in the upper 7 m (considering the exponential decay of orbital velocity with depth). Below this depth, we would expect little error in the turbulence sensor due to off axis flow even if the sensor were fixed in space. In an experiment with a submarine that does not follow the water parcel, Osborn et al. (1992), under similar surface and wind conditions to ours, estimated less than a factor 2 error at a depth of 2 m, decreasing with depth. Given that the glider follows the water parcel, the error in our study would be significantly less.

The turbulent heat equation in a simplified form can be expressed as

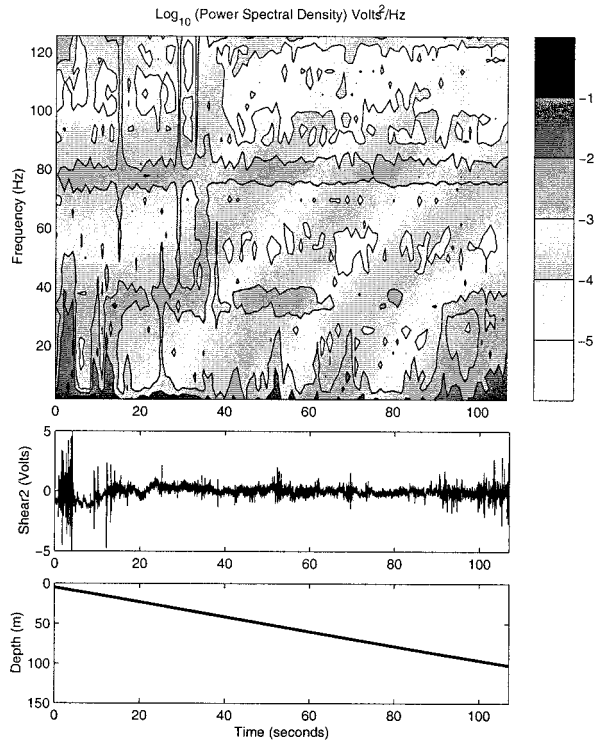


FIG. 3. (top) Spectrogram of the microstructure shear signal for EPSONDE2 station 14, profile 12. Contours have units of $\text{volts}^2 \text{Hz}^{-1}$. (middle) Time series used to generate the spectrogram shown low-pass filtered at 40 Hz for clarity. (bottom) Depth of the instrument as function of time as EPSONDE falls vertically.

$$\overline{\frac{d}{dt} \left(\frac{1}{2} T' \right)^2} = -\overline{w' T'} \frac{\partial \bar{T}}{\partial z} - \frac{1}{2} \chi_T, \quad (3)$$

where the left-hand term represents the time rate of change of temperature variance (TV). The first term on the right is the production of TV by buoyancy flux and the final term is the dissipation of TV by molecular diffusion. For isotropic turbulence, the rate of dissipation of temperature fluctuations is given by

$$\chi_T = 6D \overline{\left(\frac{\partial T'}{\partial z} \right)^2}, \quad (4)$$

where D is the molecular diffusion constant. For both instruments, χ_T is estimated from both a thermistor and a thin-film probe.

One concern in the design of EPSONDE-Glider was the additional noise introduced by the vehicle superstructure since the airfoil shear probes are very sensitive to mechanical vibration. The pressure case in which the sensors were mounted was isolated from the rest of the vehicle using open-cell urethane foam. A spectrogram of the shear signal from a profile with EPSONDE2 (vertical profiler) is shown in Fig. 3 as a standard to compare the glider against. This figure was generated using a 512-point FFT and demonstrates how the power spectral

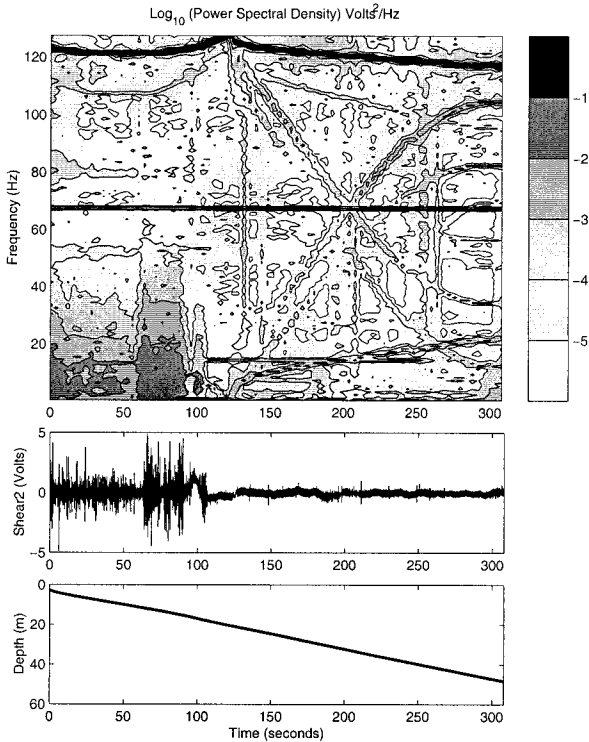


FIG. 4. Same as Fig. 3 but for EPSONDE-Glider station 9, profile 8. In this case the profile is slanted at the instrument glide angle.

density changes with time as the profiler free-falls from the surface to the seabed at 100 m. The bottom panel displays depth of the instrument as a function of time and indicates that the fall speed is nearly constant throughout the water column. The top panel shows some energy at the beginning of the profile but then decreases to a fairly constant low level until the instrument enters the bottom boundary layer where it increases once again. The dominant noise feature in this spectrogram is a constant energy source at 80 Hz. This is nearly always present in the vertical profiler signal and its broad nature is due to a resonant mechanical vibration of the pressure case. A somewhat less evident noise feature is a peak at 32 Hz that is electronic in origin due to switching in the signal multiplexor. The second panel in Fig. 3 displays a low-pass filtered (40 Hz) version of the time series used to generate the spectrogram. The depth of the mixed layer was approximately 10 m during this profile.

The shear signal from the one of the probes on EPSONDE-Glider is presented in Fig. 4. The spectrograms from both shear probes were for most cases very similar. This profile was obtained approximately two hours after the one in Fig. 3. The shear probe time series in the second panel is low-pass filtered at 40 Hz. The spectrogram in the first panel indicates mixing occurring throughout the OML with an enhancement toward the base at 15 m. This vehicle provides much-improved sampling in the OML, especially near the surface, as

compared to the vertical profiler. This spectrogram indicates very different noise characteristics for the glider when compared to the vertical profiler. The 70-Hz noise spike is quite limited in bandwidth and, therefore, easy to remove during processing of the spectra. It was discovered after this field experiment that this noise spike was due to vibrations from the glider digital gyro inclinometer that were transmitted through the glider pressure case to the shear probe. The more serious noise issue is a high-frequency spike at about 120 Hz that migrates in frequency with time. This was observed to occur predominantly between 100 and 120 Hz but in some cases was at much lower frequencies. Some energy from this spike often appeared aliased to lower frequencies. The case presented in Fig. 4 was typical of one of the more difficult profiles to process because of the contamination of the low frequencies. In most cases, the turbulent kinetic energy signal at low frequencies could be easily differentiated from the noise.

4. Results

A summary of atmospheric boundary layer measurements provided by the Minimet buoy is shown in Fig. 5 along with ocean temperature and density measurements from a CTD probe. The wind speed stick plot (a) indicates that the winds were relatively light, aside from the period (25–27 June) in which a low pressure system passed the area [indicated by the atmospheric pressure measurement in (b)]. The air–sea temperature difference (c) increased over the period of the deployment from -2° to 0°C near a mean air temperature of 12°C . The majority of this study will concentrate on two time periods during the field experiment: 1) 1600–2000 UTC 25 June 1996 and 2) 1200–2000 UCT 26 June 1996. During these periods (highlighted in Fig. 5) the air–sea temperature difference ranged from 0° to 0.6°C , indicating close to neutrally stable conditions. CTD casts were combined to provide a time series of temperature (Fig. 5d), salinity, and potential density (Fig. 5e) at the experiment site. The triangular symbols in the top panel of Fig. 5d indicate the times at which CTD casts were taken. The interpolation required during large gaps in time between casts (specifically 23–25 September) limits the accuracy of this section of the plot. During the period covered in this study the depth of the OML varied between 10 and 20 m. As is typical for the Scotian shelf in June, the temperature panel indicates summertime warming at the surface and the presence of a cold intermediate layer.

Most of the energy flux in the atmosphere is dissipated in the air before reaching the surface of the ocean. This energy flux may be expressed as

$$E_{10} = \tau U_{10} = \rho_a C_{10} U_{10}^3, \quad (5)$$

where τ is the surface wind stress, ρ_a is the air density, C_{10} is the drag coefficient, and U_{10} is the wind speed at 10-m height. Richman and Garrett (1977) used field and

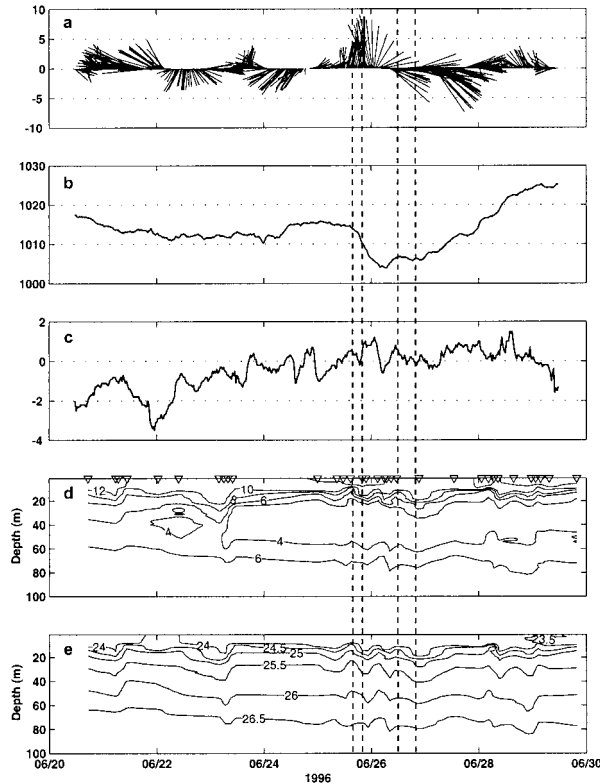


FIG. 5. Atmospheric boundary layer data collected by the Minimet buoy at $43^{\circ}30.3'N$, $62^{\circ}44.4'W$. Wind speed vectors, (a) atmospheric pressure, (b) and air-sea temperature difference (c) are plotted as a function of time. Shown in the lower panels are contoured CTD data for temperature ($^{\circ}C$) (d) and density ($kg\ m^{-3}$) (e). Triangular symbols in (d) indicate the time of CTD casts. The vertical dashed lines indicate two periods of microstructure observations: 1) 1600–2000 UTC 25 Jun 1996 and 2) 1200–2000 UTC 26 Jun 1996.

laboratory measurements in combination with a model to estimate that between 4% and 9% of the energy, including that going into wave breaking, may cross the air-sea interface. Oakey and Elliott (1982, hereafter OE82) determined that $\sim 1\%$ of E_{10} was dissipated in the OML using a vertical microstructure profiler to estimate integrated dissipation, ϵ_I , defined as

$$\epsilon_I = \int_{-h}^0 \epsilon(z) dz, \quad (6)$$

where h is the depth of the mixed layer. Oakey and Elliott stated that their estimate of the integrated dissipation in the mixed layer was likely an underestimate because they were unable to make measurements in the top 5 m of the water column. Therefore, an assumption was made that the dissipation in this part of the mixed layer was equal to the dissipation in the upper part of the OML that was measured. Using a freely rising vertical profiler, AM95 demonstrated some support for the conclusion of OE82, but questioned whether this parameterization may substantially underestimate some observed TKE dissipation rates.

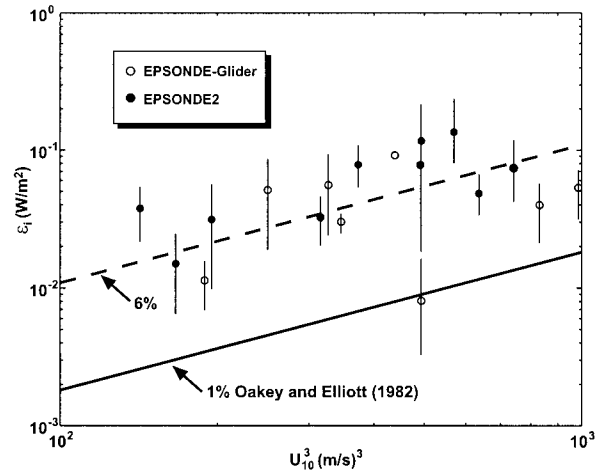


FIG. 6. Depth-integrated dissipation rate in the OML, ϵ_I , as a function of the cube of the wind speed at 10 m. Open circles represent EPSONDE-Glider data. Filled circles are for EPSONDE2 data. The error bars are calculated using a bootstrap estimate of the mean and 95% confidence intervals (Efron and Gong 1983) for the data at each wind speed.

Estimates of integrated dissipation in the OML during this field program have been made with both the vertical profiler EPSONDE2 and EPSONDE-Glider. Using (6), ϵ_I was calculated for the part of the OML measured by each instrument. This typically did not include the upper 5-m of the OML for EPSONDE2 and the upper 2 m for the EPSONDE-Glider. An assumption of the profile of dissipation in the mixed layer was made based on classical wall layer scaling, that is $\epsilon \propto z^{-1}$. The measured ϵ_I was then corrected for the portion of the mixed layer not measured to provide a total integrated dissipation for the OML.

The results of this calculation are presented in Fig. 6 where ϵ_I is plotted as a function of U_{10}^3 . The abscissa in this figure may be converted to the energy at 10 m using (5). The 10-m wind measured with the shipboard anemometer was typically obtained immediately before or after a microstructure station. There were certain cases (ship at anchor) for EPSONDE-Glider in which anemometer runs were made simultaneously with the microstructure profiles. In cases where the anemometer run was not within one hour of the microstructure profile, the data were disregarded. The results in the figure indicate a good general agreement between the two instruments with the data overlapping at similar wind speeds. This suggests that vehicle noise in the glider system does not pose a problem to measurements in the OML.

The solid line in Fig. 6 represents a fit of the data obtained by OE82 and represents $\sim 1\%$ of the wind energy at 10 m being dissipated in the OML. The ϵ_I data obtained in this field experiment are substantially larger than those measured by OE82. The differences in the two studies include 1) an improved system to make measurement in the atmospheric surface layer, 2)

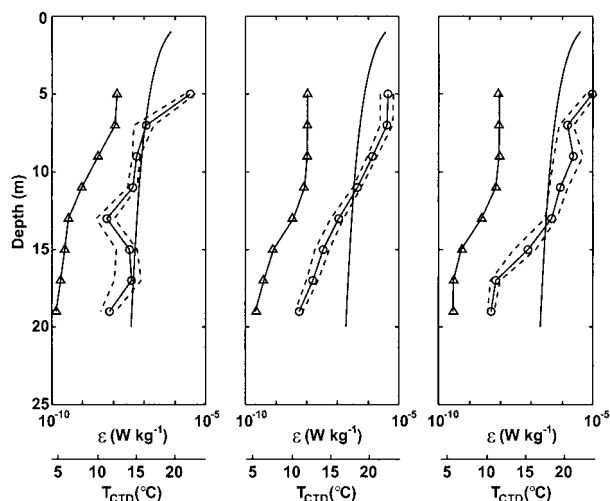


FIG. 7. Station-averaged profiles of TKE dissipation rate, ϵ , as a function of depth for the vertical profiler EPSONDE2. The circles give the bootstrap estimate of the mean with the dashed lines representing the 95% confidence intervals. The mean profile of temperature in the OML is given by the triangles. The solid line represents the wind stress production based on the shipboard bow anemometer measurements. The subplots are for (a) Station 014, (b) Station 015, and (c) Station 017 where time, date, and conditions are shown in Table 1.

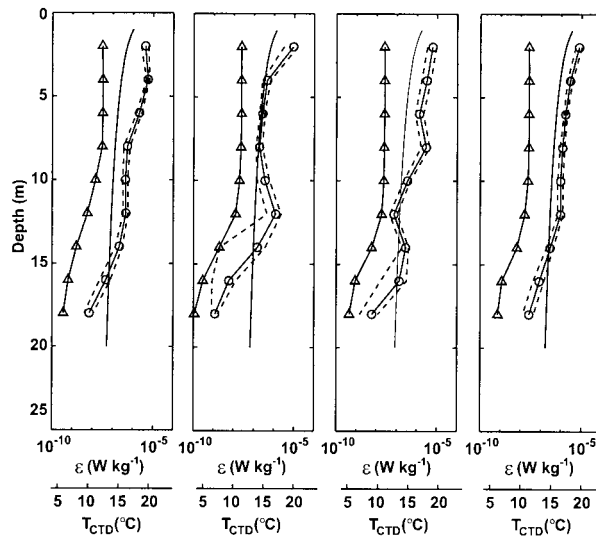


FIG. 8. Same as Fig. 7 but for EPSONDE-Glider. Subplots are for (a) Station 009, (b) Station 010, (c) Station 011, and (d) Station 012 where time, date, and conditions are shown in Table 2.

differences in surface forcing due to the time of the year in which the experiments were carried out (June for the present field study, October for OE82), and 3) different treatment of the portion of the OML not measured. Oakley and Elliott divided the measured fraction of the OML into two layers. The lower layer comprised the bottom 10 m of the OML and the upper layer represented the remaining portion to 5.5-m depth. The dissipation in the top 5.5 m of the OML was assumed to be the same as that measured in the upper OML and, hence, the total integrated dissipation was calculated as

$$\epsilon_I = \epsilon_{\text{lower}} \Delta Z_{\text{lower}} + \epsilon_{\text{upper}} (\Delta Z_{\text{upper}} + 5.5 \text{ m}). \quad (7)$$

In the current study it was not feasible to divide the OML into two layers since the depth was typically about 10 m. If the assumption that the dissipation is the same in both measured and unmeasured parts of the OML for the present study (as opposed to the wall layer scaling used to create Fig. 6), the ϵ_I values decrease by as much as a factor of 2 for the vertical profiler data. However, there still remains a significant difference from OE82.

A dashed line representing 6% of the wind energy at 10 m being dissipated in the OML has been added to this figure to represent to fraction of energy being dissipated in the OML as indicated by the data from this study. This value falls in the middle of the range suggested by Richman and Garrett (1977).

The validity of the assumption that the OML behaves as a classical wall layer has been the topic of debate recently. AM95 showed that in most cases ϵ was balanced by wind stress production of TKE. However, in some cases ϵ was greatly enhanced relative to the wind stress production and exhibited exponential decay with depth. Some representative results of the present study are shown in Fig. 7 (EPSONDE2) and Fig. 8 (EPSONDE-Glider). A common feature of all the plots in Fig. 7 is that in the mixed layer ϵ is enhanced by about one order of magnitude relative to the wind stress production. This has not been commonly observed, but there are very few open ocean datasets to our knowledge that combine accurate wind stress measurements with measurements of TKE dissipation in the mixed layer. A summary of the atmospheric boundary layer conditions for these EPSONDE2 stations is given in Table 1. The solid curves in the subplots of Fig. 7 represent $u_{*w}^3/\kappa z$ with the friction velocity obtained from the bow-ane-

TABLE 1. Atmospheric surface-layer data corresponding to Fig. 7: T_a represents the air temperature measured by the bow anemometer system on the ship, T_s is the sea surface temperature, U_{10} is the 10-m wind speed, u_{*a} is the friction velocity in air, τ is the surface wind stress, C_{10} is the 10-m drag coefficient, H_s is the significant wave height of the windsea, and F is the wind energy input parameter.

Station	Casts	Date	Start time (UTC)	T_a (°C)	$T_s - T_a$ (°C)	U_{10} (m s ⁻¹)	Wind direction		u_{*a} (m s ⁻¹)	τ (N m ⁻²)	C_{10}	H_s (m)	F (m ³ s ⁻³)
							(°T)	(°T)					
014	15	25 Jun	1513	13.6	-2	6.8	180	0.193	0.046	1.08×10^{-3}	0.55	2.20×10^{-4}	
015	15	26 Jun	0159	14.1	-0.1	8.6	8	0.381	0.177	2.02×10^{-3}	1.61	5.98×10^{-4}	
017	15	26 Jun	1030	12.9	0	10.2	261	0.399	0.194	1.57×10^{-3}	1.32	1.03×10^{-3}	

TABLE 2. Atmospheric surface-layer data corresponding to Fig. 8. Parameters are as those listed in Table 1.

Station	Casts	Date	Start time (UTC)	T_a (°C)	$T_s - T_a$ (°C)	U_{10} (m s ⁻¹)	Wind direction (°T)	u_{*a} (m s ⁻¹)	τ (N m ⁻²)	C_{10}	H_s (m)	F (m ³ s ⁻³)
009	15	25 Jun	1648	13.3	-0.7	6.9	166	0.21	0.056	1.04×10^{-3}	0.62	1.53×10^{-4}
010	3	26 Jun	1217	12.6	-0.7	7.9	244	0.259	0.082	1.15×10^{-3}	0.67	1.82×10^{-4}
011	5	26 Jun	1630	12.3	-1.9	9.1	247	0.264	0.084	1.02×10^{-3}	1.04	7.85×10^{-4}
012	14	26 Jun	1758	12.6	-1.3	9.9	246	0.322	0.127	1.15×10^{-3}	1.25	1.42×10^{-3}

nometer system. The bow anemometer runs did not overlap the microstructure profiling due to logistics. Nevertheless, these runs were acquired within 30 minutes of the start and end of each EPSONDE2 station shown in Fig. 7. The dissipation estimates were combined from both shear probes and binned at 2-m depth intervals. A bootstrap estimate (Efron and Gong 1983) of the mean for each bin appears as an open circle in the plot. The dashed lines represent a 95% confidence interval from the bootstrap calculation, which implies that the estimates of dissipation in the OML are statistically different from the classical wall layer estimate based on the friction velocity.

A check of the internal consistency of the dissipation and temperature microstructure measured with EPSONDE2 is to examine the statistical distribution of mixing efficiency, Γ , defined as

$$\Gamma = \frac{N^2}{\varepsilon} \frac{\chi_T}{2(\partial T/\partial z)^2}, \quad (8)$$

where N^2 is the buoyancy frequency, χ_T is the rate of dissipation of temperature fluctuations, and $\partial T/\partial z$ is the mean temperature gradient. The second part on the right-hand side of (8) represents the vertical eddy diffusivity, K_T . A histogram of Γ (not shown here) has a lognormal distribution with mean value of 0.26, typical of other measurements in the mixed layer. Although the “mixed layer” was very weakly stratified there was sufficient stratification to measure both ε and χ_T as well as mean gradients to allow one to determine both K_T and K_p and hence estimate Γ .

Dissipation measurements from four EPSONDE-Glider stations are presented in Fig. 8. A summary of the atmospheric boundary layer conditions for these stations is given in Table 2 along with the significant wave height of the windsea, H_s . It is obvious from the four plots that the glider is able to provide more extensive sampling of the boundary layer than the vertical profiler is because it samples to within 2 m of the ocean surface. The plot in Fig. 8a for Station 009 (25 June 1996) indicates a shallow mixed layer of 10-m depth, which is similar to that seen with EPSONDE2 one hour earlier (Station 014, Fig. 7a). During the 3-h period of this station, eight bow anemometer runs were compiled and an average of this data is presented in Table 2. The wind speed during this station varied from 5.7 to 9.2 m s⁻¹, wind direction gradually changed from 174° to 154°T, and the sea-air temperature difference ranged from -2°

to +0.5°C. The glider measurement of ε is consistent with that from the vertical profiler being approximately one order of magnitude larger than the wind stress production estimate. In addition, ε does not appear to be proportional to z^{-1} in the OML as would be expected for a classical wall layer.

On the subsequent day (26 June 1996), three EPSONDE-Glider stations were carried out over an 8-h period (Figs. 8b-d). The 10-m wind speed increased from 7.9 to 9.9 m s⁻¹ while the direction remained constant. The significant wave height of the windsea also increased from 0.67 to 1.25 m. The depth of the mixed layer for these three stations was about 13 m indicating that the OML had deepened from the previous day. The plots of dissipation versus depth for Stations 010 and 011 (Figs. 8b and 8c) comprise only 3 and 5 profiles, respectively, which limits the statistical significance of these results. This data will be combined later with Station 012, for which there were 14 casts over a 2.5-h period. A common feature of both Stations 010 and 012 is that the dissipation appears to scale with z^{-1} ; however, the magnitude relative to the wind stress production differs substantially. It is difficult to discern a similar trend in dissipation for Station 011 because of the variability in the lower part of the mixed layer.

Anis and Moum (1995) observed enhanced values of ε close to the ocean surface and attributed this to breaking waves. These observations indicated high values of ε deeper than the e -folding scales of the wind waves, leading AM95 to hypothesize that for irrotational waves this could be due to a downward transport of TKE by the swell. In the case of rotational waves, the resulting wave stresses could indirectly enhance the turbulence in the near-surface layer. Both of these mechanisms imply an exponential decay of turbulence with depth. For one of their cases, AM95 divided the OML into an upper section (1.5–5.5 m) dominated by wind waves and a lower section (5.5–14.5 m) dominated by swell. In this case there was an abrupt change in the slope of $\varepsilon(z)$ at 6 m. AM95 fit the observed dissipation rates in each section to a simple exponential form, $\varepsilon(z) = \varepsilon_o \exp(\alpha z)$, as suggested from the scaling derivations. The results suggested that wave-related turbulence was important in the upper part of OML. An exponential fit of the EPSONDE-Glider data was carried out for each station displayed in Fig. 8. Only Station 10 (Fig. 8b) indicates a change in the slope of $\varepsilon(z)$ as in AM95; however, a plot at higher vertical resolution (not shown) indicates

that above 5 m dissipation is almost constant as opposed to decaying exponentially with depth.

Terray et al. (1996) used data collected from a research platform in Lake Ontario to study OML dissipation measurements under strong wind-forcing conditions. This investigation showed a layer of enhanced dissipation in the OML exceeding wall layer values by one to two orders of magnitude. They proposed a scaling for dissipation in the OML based on wind and wave parameters in which a nondimensional ε is expressed as

$$\frac{\varepsilon H_s}{F} = 0.3 \left(\frac{z}{H_s} \right)^{-2}, \quad (9)$$

where F is the rate of energy input to the waves from the wind and H_s is the significant wave height of the windsea. In the present study, H_s is determined using data collected by the directional Waverider (DWR) buoy. This instrument provides a measure of the significant wave height of the total wave spectrum including both swell and windsea. Here H_s for the windsea only was calculated as $H_s = 4\sigma$, where σ is the square root of the variance in the portion of the wave energy spectrum related to local wind forcing. The range of frequencies used to integrate the wave spectrum was determined by finding the crossover point of the component of the 10-m wind in the direction of the wave ($U_{10} \cos\Delta\theta$) and the wave phase speed (c). The parameter $\Delta\theta$ is the angle between the direction of the 10-m wind and the waves. The variance is computed by integrating the energy from the crossover frequency to the upper limit of the instrument (0.64 Hz). The wind energy input parameter F is defined as

$$F = g \int \beta S_\eta \, d\omega \, d\theta, \quad (10)$$

where $S_\eta(\omega, \theta)$ is the frequency–direction spectrum of the wave and β is the e -folding scale for the temporal growth of wave energy with the assumption of negligible dissipation and nonlinear interactions. A formulation suggested by Donelan and Pierson (1987) that relates β at each frequency to the wind speed is given as

$$\frac{\beta}{\omega} = 0.194 \frac{\rho_a}{\rho_w} \left(\frac{U_{\pi/\kappa} \cos\theta}{c(k)} - 1 \right) \left| \frac{U_{\pi/\kappa} \cos\theta}{c(k)} - 1 \right|, \quad (11)$$

where ρ_a is the density of air, ρ_w is the water density, ω is the radian frequency, and k is the wave component wavenumber. The term $U_{\pi/\kappa} \cos\theta$ is the wind component in the wave direction evaluated at a reference height of π/κ , equivalent to one-half the wavelength. The constant, 0.194, has been empirically determined.

The Water Air Vertical Exchange Studies (WAVES) study by T96 was based on a dataset acquired in a relatively shallow (12 m) depth in Lake Ontario. Only cases of offshore winds over the short fetch of 1.1 km were considered, and this limited study to young waves

(wave age $c_p/u_{*a} \approx 4$ –7) with no swell. During SWADE, Drennan et al. (1996) extended the model of T96 to open ocean conditions. Of the 20 cases included in the study of Drennan et al. (1996), 18 had directional wave spectra that indicated a simple windsea (i.e., the swell and windsea have a well-defined spectral gap). The SWADE study had wind speeds of 9–12 m s⁻¹ and included the following ranges of wave parameters: 1) $H_s \approx 0.9$ –2.6 and 2) $c_p/u_{*a} \approx 13$ –29. One limitation of this study was that the depth of the dissipation measurements in the OML was relatively limited between 1.25 and 1.89 m. Hence, the range of variation in the parameter z/H_s (0.7–2.1) is predominantly determined by the changes in H_s .

The following analysis concentrates on data collected during two time periods: 1) 1600–2000 UTC 25 June 1996 and 2) 1200–2000 UTC 26 June 1996. The first case represents the time covering EPSONDE-Glider station 009. In this case, the ship was at anchor, head into the wind. This allowed bow anemometer runs to be performed at the same time as glider profiles were being carried out from the stern of the ship. The glider profiled slightly to the starboard side of the ship and, hence, was not directly in the ship's wake. The directions of the wind and wave fields from a representative sample of this station are shown in Fig. 9a. At low frequencies, there is little correlation between the wind and wave field because these waves are not locally forced. At frequencies above 0.25 Hz, the alignment is very good. One- and two-dimensional representations of the wave field energy density are presented in Figs. 9b and 10, respectively. As is evident in both figures, there is a well-defined spectral gap between the swell (0.11 Hz) and windsea (0.28 Hz) peaks. This facilitates an accurate estimation of the windsea energy. The wind direction as measured by the bow anemometer was 173°T, which falls in the middle of the peak in Fig. 10.

In Fig. 9b, the component of the 10-m wind in the direction of the wave field is defined as

$$U_c(f) = U_{10} \cos\Delta\theta(f), \quad (12)$$

where $\Delta\theta(f)$ is the angle between the wind and wave directions. The 10-m wind speed is plotted as a dotted line. Following Dobson et al. (1989), the separation frequency, f_s , of the windsea and swell is taken to be

$$f_s = f_c - 0.03 \text{ Hz}, \quad (13)$$

where f_c is termed the critical frequency at which the phase speed of the waves, c , equals $U_c(f)$. In this case, $f_c = 0.25 \text{ Hz}$, in good agreement with the energy density plot of the wave field. The wave growth parameter, β , can now be calculated for each frequency using (11) and, in turn, the wind input F can be determined using the directional wave spectrum as shown in Fig. 10.

The OML dissipation estimates from EPSONDE-Glider Station 009 were combined with the corresponding wave and wind data to produce Fig. 11. In this plot of scaled dissipation versus depth, the solid line rep-

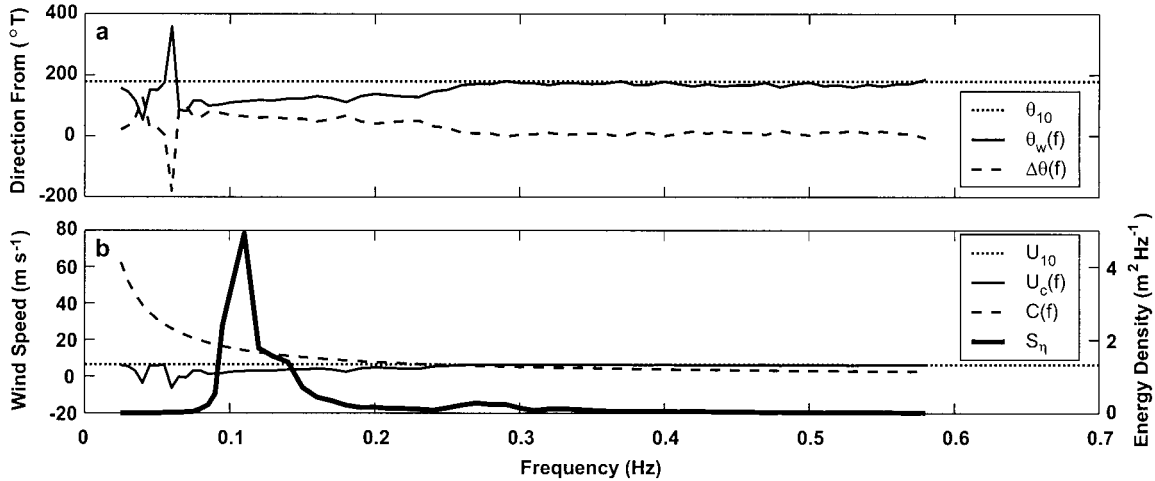


FIG. 9. In (a), the dotted line represents wind direction at 10 m as measured by bow anemometer on CSS *Parizeau* for the time period of EPSONDE-Glider station 009 profiles 004–008. The direction of the waves, $\theta_w(f)$ (solid line), and the angle between the wave and wind fields, $\Delta\theta(f)$ (dashed line). In (b) the wave power spectrum (thick solid line) is shown for the Station 009 profiles 004–008. The diagram also shows the 10-m wind speed U_{10} (dotted line), the computed wave phase speed $c(f)$ (dashed line), and the wind speed in the wave direction $U_c(f) = U_{10} \cos\Delta\theta(f)$ (thin solid line).

resents the T96 fit to the WAVES data, as given in (9). The estimates of $\varepsilon H_s/F$ for the glider data were combined into 1-m depth bins and, subsequently, a mean (circles) and 95% confidence intervals (dashed lines) were determined for each bin using a bootstrap. The solid circle in this plot is obtained from EPSONDE2 profiles carried out for this time period. The starting depth of the vertical profiler in this cases limits its comparison to the other datasets. There appears to be general agreement between the results of the present study and those of T96 with $\varepsilon \propto z^{-2}$ seeming to be a reasonable

assumption as opposed the z^{-1} predicted by a classical wall layer. The glider data is based on only 15 profiles over a 3-h period and, due to the intermittent nature of turbulence in the OML, it is not surprising to see some deviation in the results of the two studies. Additional mixing and dissipation at the base of the OML due to inertial shears may influence the results at $z/H_s \approx 10$.

On the following day, with stronger winds, data were collected for three EPSONDE-Glider stations (010–012) over a period of eight hours. A representative sam-

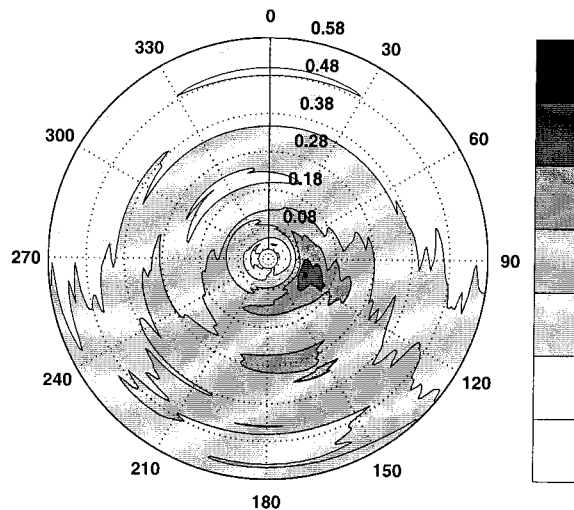


FIG. 10. Polar plot of 2D wave spectrum recorded during Station 009 profiles 004–008. Frequency increases with distance from center of plot. Swell peak observed at 0.11 Hz, 110°T. Windsea peak at 0.28 Hz, 165°T. Wind direction is 173°T. Directions are in standard meteorological convention. Contour levels are log scaled with magnitudes indicated on colorbar.

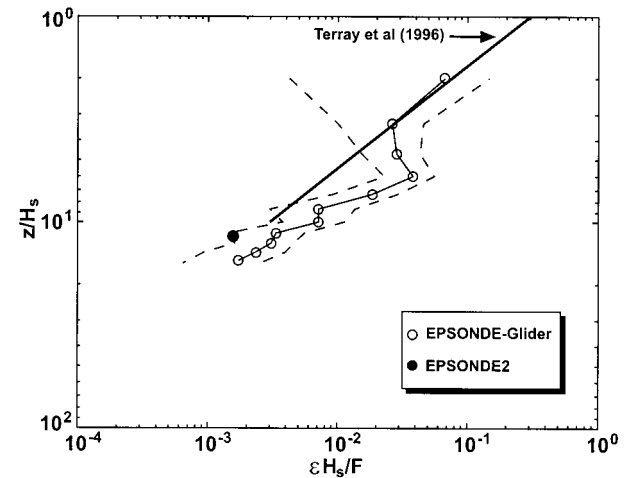


FIG. 11. Dissipation rate vs depth in the scaled coordinates of Terray et al. (1996). Ordinate represents the number of significant wave heights below the surface. Solid line represents best fit of WAVES data. The open circles represent the mean of the scaled dissipation results for all profiles in EPSONDE-Glider Station 009. Dashed lines indicate 95% confidence intervals based on a bootstrap estimation. The solid symbol is calculated using EPSONDE2 profiles during this time period.

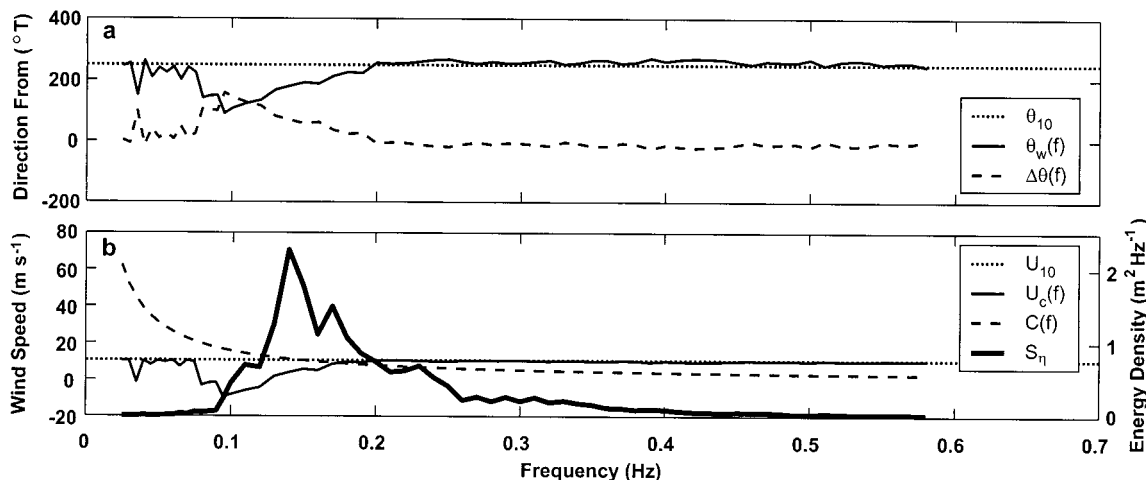


FIG. 12. Same as Fig. 9 for EPSONDE-Glider Station 012 profiles 004–009.

ple of data collected during this period has been chosen to highlight the results. The directions of the wind and wave field during Station 012 profiles 004–009 are shown in Fig. 12a. The direction of the wind as measured by the bow anemometer was 249°T. It is apparent from the plot that the two fields are beginning to align at a lower frequency than seen in Station 009. One- and two-dimensional representations of the wave field energy density are presented in Figs. 12b and 13, respectively. In contrast to the wave field for Station 009 in which there was discernable separation between swell and wind-sea, in this case the swell and wind-sea overlap. There is no well-defined spectral gap and, therefore, determining the windsea energy alone is more difficult. It appears from the energy density plot in Fig. 12b that the peak of the windsea spectrum occurs at approximately 0.23 Hz. One interesting thing to note is that the

energy spectrum in the polar plot, Fig. 13, bifurcates at high frequencies. This occurred in the majority of cases for the DWR data during these three Glider stations.

As in Fig. 11, the OML dissipation estimates from EPSONDE-Glider Stations 010–012 were combined with the corresponding wave and wind data to produce Fig. 14. The estimates of $\varepsilon H_s/F$ for the glider data were combined into 1-m depth bins and, subsequently, a mean (circles) and 95% confidence intervals (dashed lines) were determined for each bin using a bootstrap. EPSONDE2 data from this time period (solid circles) compares well with the EPSONDE-Glider results at similar z/H_s . In this case, there does not appear to be agreement between the WAVES results and the present study. While these results, also summarized in Fig. 8, indicate

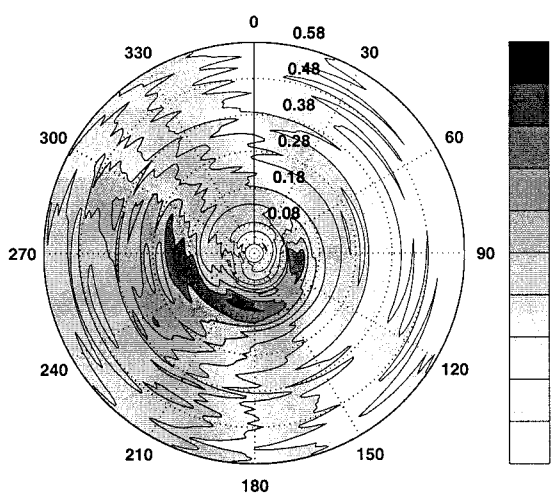


FIG. 13. Polar plot of 2D wave spectrum recorded during Station 012 profiles 004–009. Two swell peaks observed at 0.12 Hz, 100°T and 0.14 Hz, 200°T. Windsea peak appears to be at 0.23 Hz, 260°T. Wind direction is 249°T. Directions are in meteorological convention.

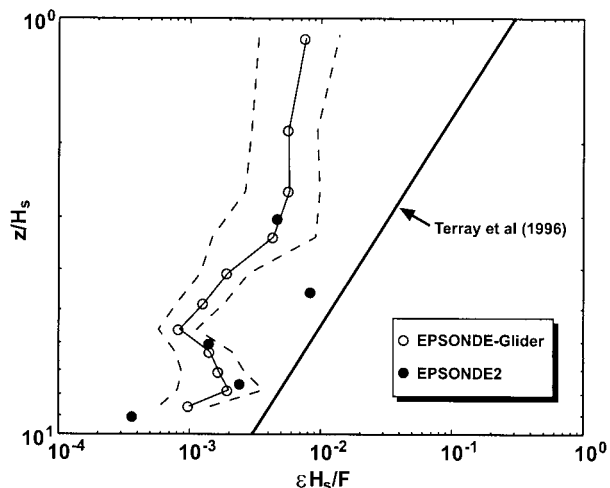


FIG. 14. Dissipation rate vs depth in the scaled coordinates of Terray et al. (1996). Solid line represents best fit of WAVES data. The circles represent the mean of the scaled dissipation results for all profiles in EPSONDE-Glider Stations 010–012. Dashed lines indicate 95% confidence intervals based on a bootstrap estimation. Solid symbols are calculated using EPSONDE2 profiles during this time period.

that the dissipation in the OML is enhanced relative to the wind stress production, the relationship of $\varepsilon \propto z^{-1}$ appears better suited than that suggested by the WAVES data. Of course, the scaling proposed by T96 makes the assumption that nonlinear wave-wave interactions are negligible as is dissipation due to wave breaking. The WAVES dataset included only cases of offshore wind that produced young waves over the 1-km fetch and, hence, did not consider any cases with swell. During SWADE, Drennan et al. (1996) provided confirmation of the WAVES parameterization in the open ocean but, once again, 18 of the 20 cases considered were those with a simple windsea. In the open ocean under strong wind forcing with the presence of swell, it appears that the parameterization of T96 breaks down. Since this is likely an important aspect of air-sea interaction, further investigation is warranted.

5. Summary

A field experiment was carried out 17–30 June 1996 on the Scotian shelf with an integrated set of measurements consisting of air-sea fluxes, surface wave spectra, and rates of dissipation of TKE, ε , in the ocean mixed layer (OML). Field studies with accurate measurements of these parameters simultaneously do not exist for open ocean conditions. Measurements of ε were obtained with a unique microstructure profiler that profiles in a quasi-horizontal manner using lift generated by a wing mounted on the vehicle. A vertical profiler, EPSONDE2, which has been used in numerous field experiments, complemented these dissipation estimates. Atmospheric boundary layer measurements were obtained with a ship-mounted bow anemometer system consisting of a propeller-vane anemometer and two fast-response thermistors. A pitch/roll buoy provided directional wave spectra.

Estimates of the integrated dissipation in the OML were made using both vertical and quasi-horizontal microstructure profilers. These results were corrected by assuming that in the upper portion of the OML not measured by these instruments (5 m for EPSONDE2 and 2 m for EPSONDE-Glider) that $\varepsilon \propto z^{-1}$ as suggested by classical wall layer theory. The results indicate that ~6% of the wind energy at 10 m is dissipated in the OML. This is in contrast to the results of Oakey and Elliott (1982) in which they found the fraction to be 1%. Nevertheless, this is in agreement with the study of Richman and Garrett (1977), which predicted values in the range of 4%–9%.

The results for this study have been used to test the proposed scaling of dissipation with depth based on wind and wave parameters measured during the WAVES experiment in Lake Ontario (Terray et al. 1996). This scaling was confirmed for open ocean conditions by Drennan et al. (1996) but many of those cases were for simple wind sea conditions. Using data collected with EPSONDE-Glider, the bow anemometer, and the Wave-

rider, we have found that the WAVES scaling holds for the case of a simple windsea in which the swell can be easily separated. In more complex situations in which the windsea cannot be easily discerned because of interactions with the swell, ε remains enhanced relative to the wind stress production; however, the proposed scaling that decays as z^{-2} does not hold. The scaling of Terray et al. (1996) neglects wave-wave interactions and dissipation and, hence, would not be expected to hold for such complex open ocean conditions. However, these conditions are common and important to air-sea interaction, so the use of the WAVES scaling would not be valid for many cases in the open ocean.

Due to a combination of technical difficulties and extremely calm weather, the amount of data collected during our field program is limited. This data, nevertheless, has provided an important addition to our understanding of the relationship between dissipation of TKE in the OML and the wind and wave fields. It would suggest that further investigations are necessary to understand these open ocean relationships especially in the presence of swell.

Acknowledgments. This program was partially funded by the U.S. Office of Naval Research (N00014-93-1-0522). The authors would like to thank the following people at the Bedford Institute of Oceanography: Scott Young, Lisa Clark, Jean-Guy Dessereault, Bob Ryan, Bob Anderson, George Steeves, John Conrod, Mike LaPierre, Jack Horne, Garon Awalt, Glen Morton, Brian Beanlands, Liam Petrie, Murray Scotney, and the crew of the CSS *Parizeau*. The authors would also like to acknowledge the contributions of Jeff Scrutton and Scott McLean (Satlantic Inc.); Walter Judge, Phil MacAulay, and Elizabeth Gonzalez (Dalhousie University); and Richard Goldsworthy (Defense Research Establishment Atlantic). Thanks also to Will Perrie and the two reviewers for their advice on the manuscript.

REFERENCES

- Agrawal, Y. C., E. A. Terray, M. A. Donelan, P. A. Hwang, A. J. Williams III, W. M. Drennan, K. K. Kahma, and S. A. Kitai-gorodskii, 1992: Enhanced dissipation of kinetic energy beneath surface waves. *Nature*, **359**, 219–220.
- Anderson, R. J., 1993: A study of wind stress and heat flux over the open ocean by the inertial-dissipation method. *J. Phys. Oceanogr.*, **23**, 2153–2161.
- Anis, A., and J. N. Moum, 1992: The superadiabatic surface layer of the ocean during convection. *J. Phys. Oceanogr.*, **22**, 1221–1227.
- , and —, 1995: Surface wave-turbulence interactions: Scaling $\varepsilon(z)$ near the sea surface. *J. Phys. Oceanogr.*, **25**, 2025–2045.
- Churchill, J. H., and G. T. Csanady, 1983: Near-surface measurements of quasi-Lagrangian velocities in open water. *J. Phys. Oceanogr.*, **13**, 1669–1680.
- Dillon, T. M., J. G. Richman, C. G. Hansen, and M. D. Pearson, 1981: Near surface turbulence measurements in a lake. *Nature*, **290**, 390–392.
- Dobson, F. W., W. Perrie, and B. Toulany, 1989: On the deep-water

- fetch laws for wind-generated surface gravity waves. *Atmos.–Ocean*, **27**, 210–236.
- , S. D. Smith, and R. J. Anderson, 1994: Measuring the relationship between wind stress and sea state in the open ocean in the presence of swell. *Atmos.–Ocean*, **32**, 237–256.
- Donelan, M. A., and W. J. Pierson Jr., 1987: Radar scattering and equilibrium ranges in wind-generated waves with application to scatterometry. *J. Geophys. Res.*, **92**, 4971–5029.
- Drennan, W. M., M. A. Donelan, E. A. Terray, and K. B. Katsaros, 1996: Oceanic turbulence dissipation measurements in SWADE. *J. Phys. Oceanogr.*, **26**, 808–815.
- Efron, B., and G. Gong, 1983: A leisurely look at the bootstrap, the jackknife and cross-validation. *Amer. Stat.*, **37**, 36–48.
- Gargett, A. E., 1989: Ocean turbulence. *Annu. Rev. Fluid Mech.*, **21**, 419–451.
- Gemmrich, J. R., and D. M. Farmer, 1999: Near-surface turbulence and thermal structure in a wind-driven sea. *J. Phys. Oceanogr.*, **29**, 480–499.
- Greenan, B. J. W., and N. S. Oakey, 1999: A tethered free-fall glider to measure ocean turbulence. *J. Atmos. Oceanic Technol.*, **16**, 1545–1555.
- Gregg, M. C., 1987: Structures and fluxes in a deep convecting mixed layer. *Dynamics of the Ocean Mixed Layer*, P. Müller and D. Henderson, Eds., Hawaii Institute of Geophysics, Special Publication, 1–23.
- Jones, I. S. F., and B. C. Kenney, 1977: The scaling of velocity fluctuations in the surface mixed layer. *J. Geophys. Res.*, **82**, 1392–1396.
- Kitaigorodskii, S. A., M. A. Donelan, J. L. Lumley, and E. A. Terray, 1983: Wave–turbulence interaction in the upper ocean. Part II: Statistical characteristics of wave and turbulent components of the random velocity field in the marine surface layer. *J. Phys. Oceanogr.*, **13**, 1988–1999.
- Lombardo, C. P., and M. C. Gregg, 1989: Similarity scaling of viscous and thermal dissipation in a convecting surface boundary layer. *J. Geophys. Res.*, **94**, 6273–6284.
- Lygre, E., and H. E. Krogstad, 1986: Maximum entropy estimation of the directional distribution of ocean wave spectra. *J. Phys. Oceanogr.*, **16**, 2052–2060.
- Oakey, N. S., 1988: EPSONDE: An instrument to measure turbulence in the deep ocean. *IEEE J. Oceanic Eng.*, **13**, 124–128.
- , and J. A. Elliott, 1982: Dissipation within the surface mixed layer. *J. Phys. Oceanogr.*, **12**, 171–185.
- Osborn, T. R., and W. T. Crawford, 1980: An airfoil probe for measuring turbulent velocity fluctuations in the water. *Air Sea Interactions: Instruments and Methods*, F. Dobson, L. Hasse, and R. Davis, Eds., Plenum, 369–386.
- , D. M. Farmer, S. Vagle, S. A. Thorpe, and M. Cure, 1992: Measurements of bubble plumes and turbulence from a submarine. *Atmos.–Ocean*, **30**, 419–440.
- Richman, J., and C. Garrett, 1977: The transfer of energy and momentum by the wind to the surface mixed layer. *J. Phys. Oceanogr.*, **7**, 876–881.
- Smith, S. D., 1980: Wind stress and heat flux over the ocean in gale force winds. *J. Phys. Oceanogr.*, **10**, 709–726.
- Soloviev, A. V., N. V. Vershinsky, and V. A. Bezverchnii, 1988: Small scale turbulence measurements in the thin surface layer of the ocean. *Deep-Sea Res.*, **35**, 1859–1874.
- Terray, E. A., M. A. Donelan, Y. C. Agrawal, W. M. Drennan, K. K. Kahma, A. J. Williams III, P. A. Hwang, and S. A. Kitaigorodskii, 1996: Estimates of kinetic energy dissipation under breaking waves. *J. Phys. Oceanogr.*, **26**, 792–807.